An in-depth study of Sn substitution in Li-rich/Mn-rich NMC as a cathode material for Li-ion batteries

Dalton Transactions

An international journal of inorganic chemistry

Accepted Manuscript

This article can be cited before page numbers have been issued, to do this please use: A. Paulus, M. Hendrickx, M. Bercx, O. Karakulina, M. Kirsanova, D. Lamoen, J. Hadermann, A. Abakumov, M. K. Van Bael and A. Hardy, *Dalton Trans.*, 2020, DOI: 10.1039/D0DT01047B.

ROYAL SOCIETY OF CHEMISTRY

rsc.li/dalton

View Article Online
DOI: 10.1039/D0DT01047B

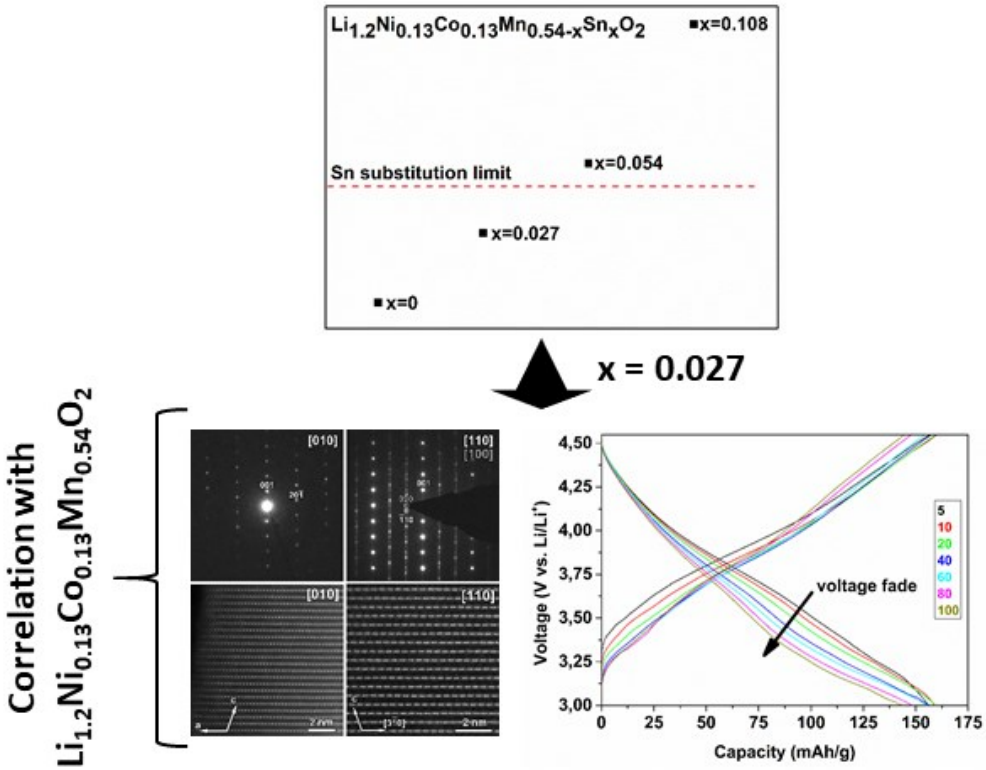

View Article Online
DOI: 10.1039/D0DT01047B

ARTICLE

An in-depth study of Sn substitution in Li-rich/Mn-rich NMC as a cathode material for Li-ion batteries

Received 00th January 20xx,
Accepted 00th January 20xx

DOI: 10.1039/x0xx00000x

Andreas Paulus,*[a,b] Mylène Hendrickx [c], Marnik Bercx[c], Olesia M. Karakulina[c], Maria A. Kirsanova[d], Dirk Lamoen[c], Joke Hadermann[c], Artem M. Abakumov[c,d], Marlies K. Van Bael[a,b] and An Hardy *[a,b]

Layered Li-rich/Mn-rich NMC (LMR-NMC) is characterized by high initial specific capacities of more than 250 mAh/g, lower cost due to a lower Co content and higher thermal stability than $LiCoO_2$. However, its commercialisation is currently still hampered by significant voltage fade, which is caused by irreversible transition metal ion migration to emptied Li positions via tetrahedral interstices upon electrochemical cycling. This structural change is strongly correlated with anionic redox chemistry of the oxygen sublattice and has a detrimental effect on electrochemical performance. In a fully charged state, up to 4.8 V vs. Li/Li$^+$, Mn^{4+} is prone to migrate to the Li layer. The replacement of Mn^{4+} for an isovalent cation such as Sn^{4+} which does not tend to adopt tetrahedral coordination and shows a higher metal-oxygen bond strength is considered to be a viable strategy to stabilize the layered structure upon extended electrochemical cycling, hereby decreasing voltage fade. The influence of Sn^{4+} on the voltage fade in partially charged LMR-NMC is not yet reported in literature, and therefore, we have investigated the structure and the corresponding electrochemical properties of LMR-NMC with different Sn concentrations. We determined the substitution limit of Sn^{4+} in $Li_{1.2}Ni_{0.13}Co_{0.13}Mn_{0.54-x}Sn_xO_2$ by powder X-ray diffraction and transmission electron microscopy to be $x \approx 0.045$. The limited solubility of Sn is subsequently confirmed by density functional theory calculations. Voltage fade for x = 0 and x = 0.027 have been comparatively assessed within the 3.00 V - 4.55 V (vs. Li/Li$^+$) potential window, from which it is concluded that replacing Mn^{4+} by Sn^{4+} cannot be considered as a viable strategy to inhibit voltage fade within this window, at least with the given restricted doping level.

Introduction

Among the rock salt type layered cathode materials for Li-ion batteries, lithium-rich/manganese-rich lithium nickel manganese cobalt oxides (LMR-NMC, xLi_2MnO_3-(1-x)$LiMO_2$ (M = Mn, Ni, Co)) are considered as a promising alternative for the commercialised $LiCoO_2$ due to their higher initial specific capacities reaching more than 250 mAh/g,(1),(2),(3),(4),(5),(6) lower cost(7),(6) and higher thermal stability(4).(8) However, commercial deployment of LMR-NMCs is impeded by voltage decay (a gradual decrease of the discharge voltage reducing the specific energy), voltage hysteresis (voltage difference on subsequent charge and discharge, penalizing energy efficiency) and sluggish (de)intercalation kinetics compromising the battery power.(9) Nowadays, it is understood that these drawbacks are intrinsic to the crystal and electronic structure of Li-rich NMC. For example, $Li_{1.2}Ni_{0.13}Mn_{0.54}Co_{0.13}O_2$ demonstrates a high reversible capacity exceeding 250 mAh/g, and only part of it (up to 170 mAh/g) originates from the $Ni^{2+} \rightarrow Ni^{3+,4+}$ and $Co^{3+} \rightarrow Co^{4+}$ cationic redox reactions, whereas a significant contribution comes from the reversible anionic redox processes ($2O^{2-} \rightarrow O_2^{n-}$, with $3 > n > 1$) above the potential of 4.5 V vs. Li/Li$^+$.(10),(11),(12),(13),(14),(15),(16),(17) Several mechanisms to stabilize the partially oxidized oxygen species have been proposed, but there is no clarity yet on the electronic and structural mechanisms of stabilization of the oxidized oxygen in the highly charged Li-rich layered oxides.(18),(19),(20),(21),(22)

The structural changes associated with the oxygen redox are also closely related to the cation migration that occurs during Li deintercalation.(23) If the material is charged to >4.5 - 4.6 V vs. Li/Li$^+$, a substantial fraction of the transition metal cations migrates to the emptied Li positions and then returns back upon discharge. However, this migration is not fully reversible, and some transition metal cations remain trapped at the octahedral Li positions and/or tetrahedral interstices. In Li-rich NMCs these defects accumulate, causing a gradual transformation of the layered structure to a spinel-like structure.(24),(25),(26),(27),(28) Most important is a conjecture that the coupled oxygen redox/cation migration causes the voltage hysteresis, whereas the partial irreversibility of the cation migration causes the voltage fade.(17) Molecular dynamics simulations of the fully charged Li-rich NMC structure suggest that formation of the peroxo-species with the O-O distance of 1.3-1.7 Å opens up the window for Mn migration to the Li layer.(29),(30) Indeed, neutron powder diffraction on $Li_{1.2}Mn_{0.55}Ni_{0.15}Co_{0.1}O_2$ reflects Mn migration

[a] Hasselt University, Institute for Materials Research (imo-imomec) and imec, division imomec, Partner in EnergyVille, DESINe team, Agoralaan Gebouw D, 3590 Diepenbeek, Belgium.
[b] EnergyVille, Thor Park 8320, 3600 Genk, Belgium.
[c] University of Antwerp, Electron Microscopy for Materials Science (EMAT), Groenenborgerlaan 171, 2020 Antwerpen, Belgium.
[d] Center for Energy Science and Technology, Skolkovo Institute of Science and Technology, 3 Nobel Street, Moscow 143026, Russia
† Footnotes relating to the title and/or authors should appear here.
Electronic Supplementary Information (ESI) available: [details of any supplementary information available should be included here]. See DOI: 10.1039/x0xx00000x

to the octahedral Li sites through intermediate population of the tetrahedral interstices.(26) Partial substitution of redox inactive isovalent cations for Mn^{4+} showing a higher M-O bond strength, is suggested as a viable strategy for stabilizing the layered structure upon charging/discharging, hereby improving the electrochemical performances. Examples of potential candidates are Sn^{4+}, Ti^{4+} and Zr^{4+}.(1),(5),(31),(32),(33)

Sn^{4+} is believed to act as a structure stabilizer, as Sn^{4+} is not easily reduced to Sn^{2+} and does not tend to adopt tetrahedral coordination.(34) As such, substitution of Sn^{4+} for Mn^{4+} is considered as a potential way to decrease the voltage fade of Li-rich/Mn-rich NMC. The substitution of Sn^{4+} for Mn^{4+} has already been reported for Ni-rich NMC ($Li[Ni_{0.82}Co_{0.12}Mn_{0.06}]_{1-x}Sn_xO_2$)(31), Li-rich/Mn-rich LNMO (Sn-stabilized $Li[Li_{0.17}Ni_{0.25}Mn_{0.58}]O_2$(34) and Li-rich/Mn-rich NMC ($Li_{1.2}Ni_{0.13}Mn_{0.54}Co_{0.13}O_2$)(35). All authors observed an enhanced reversible performance, which has been ascribed to the stabilization of the lattice upon electrochemical cycling. Lower discharge capacities as compared to the pristine materials are observed, as explained by Sn preserving its 4+ oxidation state. The significantly larger ionic radius of octahedrally coordinated Sn^{4+} (0.69 Å) than of Mn^{4+} (0.53 Å) can be considered as a double-edged sword. Its larger size could enhance lithium diffusion as it broadens intercalation pathways.(34) On the other hand, due to the large mismatch in ionic radii only a limited percentage of Mn^{4+} is expected to be replaced by Sn^{4+} in order to still retain the structure of pristine (Li-rich) NMC or LNMO.

Despite that Sn substitution in Li-rich/Mn-rich NMC (LMR-NMC) has already been reported in literature(35), neither a structural investigation probing the Sn substitution limit, nor the influence of Sn^{4+} on voltage fade in partially charged LMR-NMC were reported yet. In this paper, we have assessed the Sn substitution limit for $Li_{1.2}Ni_{0.13}Co_{0.13}Mn_{0.54-x}Sn_xO_2$ and its origin using the combination of powder X-ray diffraction, transmission electron microscopy and calculations within the Density Functional Theory (DFT) formalism. The effect of Sn substitution on the voltage fade was determined using galvanostatic cycling. $Li_{1.2}Ni_{0.13}Co_{0.13}Mn_{0.54}O_2$ was selected, as this composition is reported to demonstrate the best capacity within the Li-rich/Mn-rich NMC family(24),(8).

Experimental

Synthesis procedure

Co-precipitation route

$Li_{1.2}Ni_{0.13}Co_{0.13}Mn_{0.54-x}Sn_xO_2$ (x = 0-0.54) samples were prepared by a carbonate co-precipitation method followed by calcination. The co-precipitation reaction was performed in a stirred Globe batch reactor (Syrris Ltd., UK) under N_2 atmosphere at 60 °C. Stoichiometric amounts of $NiSO_4.7H_2O$, $CoSO_4.7H_2O$, $MnSO_4.H_2O$ and $SnSO_4$ (all – Ruskhim, ≥ 99 %.) are dissolved in distilled water. On forehand, the water content has been determined via TGA measurements (Netzsch STA 449 F3 Jupiter). The mixture with a total metal ion concentration of 2 mol/L was added dropwise at room temperature simultaneously with a 2 mol/L Na_2CO_3 (Ruskhim, 99.5 %) solution at a fixed rate of 1 mL/min into the reactor (preheated at 60 °C) under continuous stirring whilst adjusting the pH to stay constant at 7.5 by addition of dilute NH_3 (Khimmed, puriss. p.a. ≥ 25% NH_3 in H_2O) or H_2SO_4 (Khimmed, 98 w. % H_2SO_4 in H_2O). After six hours the stirrer and temperature controller were automatically switched off. The resulting precipitate was washed by distilled water and centrifuged for three minutes at 5700 rpm for three times. After drying at 75 °C overnight in a vacuum furnace, the intermediate precipitates NMC (x = 0), NMCS5 (x ~ 0.027), NMCS10 (x ~ 0.054) NMCS20 (x ~ 0.108) and NCS (x ~ 0.54) were obtained. These intermediate precipitates were dry mixed with Li_2CO_3 (Sigma Aldrich, anhydrous ≥99%). An excess of 10 mol % Li_2CO_3 was added over the stoichiometric amount to compensate for lithium loss during calcination. After grinding, the samples were consecutively calcined at a heating rate of 5 °C/min up to 500 °C with an isothermal period for 5 hours. Then they were naturally cooled down, grinded again for 15 min by mortar and pestle, and calcined at a heating rate of 5 °C/min up to 900 °C with an isothermal period for 12 hours in a tube furnace. The heating step up to 500 °C was performed under a dynamic dry air (AirLiquide, α1, 99.999%) atmosphere. The isothermal period at 500 °C and the full calcination at 900 °C were performed under static ambient air. The resulting products LNMC (x=0), LNMCS5 (x=0.027), LNMCS10 (x=0.054), LNMCS20 (x = 0.108) and LNCS (x=0.54), were grinded after naturally cooling down to room temperature and stored in closed glass vials sealed with parafilm under ambient air for further use.

Solution-gel route

$Li_{1.2}Ni_{0.13}Co_{0.13}Mn_{0.432}Sn_{0.108}O_2$ was prepared via an aqueous solution-gel method. Aqueous Li(I) citrate, $Ni(NO_3)_2$, $Co(NO_3)_2$ and $Mn(NO_3)_2$ monometal precursors were obtained by dissolving respectively $Li_3C_6H_5O_7.xH_2O$ (Sigma Aldrich, 97%), $Ni(NO_3)_2.6H_2O$ (Sigma Aldrich, ≥97%), $Co(NO_3)_2.6H_2O$ (Alfa Aesar, ≥98%) $Mn(NO_3)_2.xH_2O$ (Sigma Aldrich, 98%) in Milli-Q water. An aqueous Sn(IV) peroxocitrato monometal precursor has been prepared by adapting the protocol published by Stanulis et al(36). The final pH of the Sn(IV) peroxocitrato precursor was set at ~6.8 instead of ~7-8 reported by Stanulis et al. SnC_2O_4 (Sigma Aldrich, 98%), citric acid ($C_6H_8O_7$, Sigma Aldrich, 99%), NH_3 (Merck, extra pure, 32%) and H_2O_2 (Merck, 35%) were used as reagents. By inductively coupled plasma coupled with atomic emission spectroscopy (ICP-AES, Optima, 3300 DV, PerkinElmer) the concentrations of the monometal precursors were determined. Consecutively, citric acid ($C_6H_8O_7$, Sigma Aldrich, 99%) was added to an aqueous mixture containing stoichiometric amounts of before mentioned metals in a 1.5:1 citric acid:TM molar ratio (TM = transition metal ion). A lithium excess of 10 molar % has been used to compensate for the loss of volatile Li-containing products at elevated calcination temperatures. After stirring for about 15 min at room temperature to dissolve the citric acid, the pH was increased till ~7 by dropwise addition of NH_3 (Merck, extra pure, 32%). The resulting mixture was refluxed at 80 °C for 1 hour.

Afterwards, the mixture was placed in an oven for gelation under atmospheric conditions at 60 °C overnight. The obtained viscous gel was pre calcined under atmospheric conditions at 200 °C. The grinded pre calcined brown-colored powder was decomposed and calcined in a tube furnace using the same protocol as for the samples synthesized via the co-precipitation method described above.

Physical characterization

The samples were characterized by powder X-ray diffraction (PXRD), selected area electron diffraction (SAED), scanning transmission electron microscopy (STEM) in high-angle annular dark-field (HAADF) and annular bright field (ABF) modes and also coupled with energy-dispersive X-ray analysis (EDX).

PXRD patterns were recorded on a Huber G670 Guinier diffractometer making use of Cu Kα1 radiation. In exception, the PXRD patterns presented in **Fig. S3.** were recorded on a Bruker D8 Advance equipped with energy-dispersive LYNXEYE XY detector and operated on Cu $K_{\alpha1}/K_{\alpha2}$ radiation. The PXRD data were analyzed using the Le Bail refinement, as implemented in the JANA2006 software package.(37) The samples for SAED, STEM and STEM-EDX were made by crushing the powder in ethanol and subsequently dispersing it in this solution using an ultrasonic bath. The powder used for the particle size investigation was not crushed. A few droplets of the obtained suspension were deposited on a Cu grid covered with a holey carbon layer. The SAED patterns were recorded with a Philips CM 20, the HAADF-STEM and ABF-STEM images were acquired with an FEI Titan 80-300 "cubed" microscope operated at 300 kV, and the STEM-EDX mapping was acquired at an FEI Osiris microscope equipped with a Super-X detector and operated at 200 kV.

Density functional theory calculations

The Sn-substituted structures were constructed based on a 2x2x2 supercell of the O3-Li_2MnO_3 structure. All Mn-Li-Sn configurations were generated using the enumeration algorithm developed by Hart et al.(38–40) First, the honeycomb ordering of the Mn atoms was retained by substituting the Li atoms in the honeycomb layer by Li and Mn, restricting the stoichiometry to $Li_{1.2}Mn_{0.8}O_2$ (Note that due to the constraints of the unit cell, the actual stoichiometry is closer to $Li_{1.2083}Mn_{0.7917}O_2$, but the numbers have been rounded to simplify the notation). Second, all Sn substituted structures were generated for each Li-Mn configuration, where the Sn concentration was restricted to $x < 0.25$. Within the 2x2x2 supercell, this corresponds to a set of 5 different values for x: {i/24 | i = 1, 2, 3, 4, 5}. Depending on the Sn concentration, the algorithm generates up to thousands of configurations. Hence, for each Sn concentration, 40 different Mn-Sn orderings were considered, the geometry was optimized and subsequently the energy was calculated by a static calculation. All calculations were performed within a workflow based on the Fireworks(41) package; computational parameters are given below.

The formation energies of Sn-substituted structures for a range of x-values have been calculated within the DFT framework, as implemented in the Vienna ab initio simulation package(42–44) (VASP). The projector augmented wave (PAW) method(45) was used to make a distinction between the core and valence electrons, with the standard VASP recommended choice for the number of valence electrons. The exchange-correlation energy was calculated using the SCAN+rVV10(46,47) functional to include the van der Waals interaction, which is especially important for a layered structure such as SnO.(48) The wave functions of the valence electrons are expanded in a plane wave basis set, using a high energy cutoff equal to 500 eV, which is advisable for structures containing oxygen. For all 2x2x2 supercell calculations, a 3x3x3 Monkhorst-Pack(49) mesh was used for sampling the Brillouin zone, whereas a 6x6x3 and 9x9x7 mesh were used for Li_2SnO_3 and SnO, respectively. Geometry optimizations were performed with a Gaussian smearing of 0.05 eV, followed by a static calculation using the tetrahedron method,(50) for a precise calculation of the total energies. The convergence criterion on the electronic optimization is set at 10^{-4} eV, and 10^{-3} eV for the geometric optimization. The ways the structures and workflows are set up is explained in the Jupyter notebooks provided in the electronic supplementary material.

Electrochemical characterization

Electrochemical characterization has been performed on the final products in the coin cells type CR 2025. The active cathode material was ball milled (Retsch Emax) together with carbon black (Imerys, Super C65) and polyvinylidenedifluoride (PVDF, Alfa Aesar) as a binder in N-methyl pyrrolidone (NMP, Alfa Aesar) as the solvent in a weight ratio of 80:10:10 at 500 rpm for 30 minutes to obtain a slurry. By tapecasting the slurry in ambient atmosphere on an aluminum current collector foil with a wet coating thickness of ~150 µm and after subsequent evaporation of the NMP solvent in a vacuum furnace for 30 min at 110 °C a coating is obtained.

Cathode punches were dried under vacuum in a Büchi glass oven at 110 °C overnight to remove adsorbed water and subsequently inserted under vacuum in a glovebox. Coin cells were assembled in an Argon-filled glovebox (Sylatech). A typical half cell was obtained by separating a cathode punch and Li metal (Sigma Aldrich, 99.9% trace metals purity) as the anode by a Celgard 2400 porous polypropylene separator. 1M $LiPF_6$ in EC:DMC (50/50 (v/v)% ethylene carbonate:dimethyl carbonate, Sigma Aldrich) was used as electrolyte. After preparation and prior to cycling the coin cell type half cells have rested for 24 hours to enhance the wetting of the electrode materials and separator by the electrolyte. Galvanostatic cycling was performed between respectively 3.0 and 4.55 V vs. Li/Li^+ at C-rates of C/20 during the initial two cycles and C/10 during the subsequent cycles using a Bio-Logic BCS-805 battery tester. The electrochemical measurements have been performed at ~22 °C.

Results and discussion

Substitution range and crystal structure

The powder XRD patterns of the $Li_{1.2}Ni_{0.13}Co_{0.13}Mn_{0.54-x}Sn_xO_2$ samples LNMC (x=0), LNMCS5 (x=0.027), LNMCS10 (x=0.054), LNMCS20 (x=0.108) and LNCS (x=0.54) synthesized via the co-precipitation route (see Experimental section) are depicted in **Fig. 1.** The sharp peaks are associated with well crystallized materials.

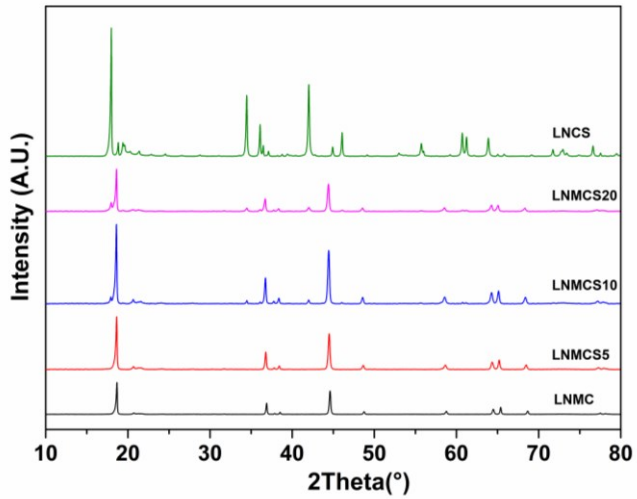

Fig. 1. PXRD patterns of LNMC (x=0), LNMCS5 (x=0.027), LNMCS10 (x=0.054), LNMCS20 (x=0.108) and LNCS (x=0.54)

Within the x range of 0 to 0.108 the strongest peaks in the patterns can be ascribed to the monoclinic *C2/m* structure typical for LMR-NMCs. The unit cell parameters refined with the Le Bail method are listed in **Table 1**.

	LNMC	LNMCS5	LNMCS10	LNMCS20
a **(Å)**	4.9360(2)	4.9507(2)	4.9560(2)	4.9668(4)
b **(Å)**	8.5479(3)	8.5699(3)	8.5780(4)	8.5806(5)
c **(Å)**	5.0172(2)	5.0265(2)	5.0417(4)	5.0345(4)
β (°)	109.017(3)	108.969(4)	109.302(4)	109.305(6)
V (Å³)	200.133(9)	201.6781(9)	202.2875(9)	202.4966(1)

Table 1. Cell parameters of LNMC (x=0), LNMCS5 (x=0.027), LNMCS10 (x=0.054) and LNMCS20 (x=0.108)

The samples demonstrate an increase in unit cell parameters and volume, concomitant with increasing the nominal Sn content that is associated with the larger ionic radius of Sn^{4+} (0.69Å) as compared to Mn^{4+} (0.53Å). However, in spite of the systematic unit cell volume change, admixture reflections appear in the powder XRD patterns starting from x = 0.054, whose intensity grows together with x. This admixture phase becomes dominant in the LNCS sample and was identified as Li_2SnO_3(51). Thus, the real substitution degree was smaller than the nominal Sn content and has been assessed with the EDX analysis. Mixed (Ni, Mn, Co, (Sn)) elemental maps of the LNMC and LNMCS5 samples and the LNMCS10 and LNMCS20 samples are presented in **Fig. 2.** The unsubstituted LNMC material consists of a single phase showing a homogeneous transition metal distribution. Its derived TM ratio, $Ni_{0.14(2)}Mn_{0.53(3)}Co_{0.13(2)}$, is in agreement with the expected stoichiometry. The Ni, Mn, Co and Sn distribution in the LNMCS5 sample appears to be very homogeneous with the atomic metal ratio of $Ni_{0.14(1)}Mn_{0.51(2)}Sn_{0.033(5)}Co_{0.13(1)}$ confirming that Sn preferentially substitutes Mn in the LMR-NMC structure. No admixture phase has been detected. The majority of the crystallites in the LNMCS10 sample are also very homogeneous, providing the cation composition of $Ni_{0.13(1)}Mn_{0.49(2)}Sn_{0.044(6)}Co_{0.13(1)}$. However, small Sn-rich crystals are already present indicating exsolution of the Sn-rich phase. The LNMCS20 sample consists of two phases: one is LMR-NMC with the $Ni_{0.14(1)}Mn_{0.48(2)}Sn_{0.04(1)}Co_{0.14(1)}$ cation composition and homogeneity identical to the LMR-NMC phase in the LNMCS10 sample within the standard deviation, and another one is $(Ni_{0.06(1)}Mn_{0.07(4)}Sn_{0.85(6)}Co_{0.01(2)})$. As there were no particles observed by STEM-EDX showing exclusively a Sn content and as the Ni, Mn and Co content of the Sn-rich admixture phase detected is very low relative to the Sn content it has been concluded that the admixture phase is Li_2SnO_3 most probably co-doped with the beforementioned transition metals. From the LNMCS10 and LNMCS20 samples it can be concluded that the Sn for Mn replacement does not exceed $x \approx 0.045$. The particle size distribution plots (**Fig. S2**.), values for mean, minimum and maximum particle sizes (**Table S1.**) and the corresponding HAADF-STEM images (**Fig. S1.**) for the LNMC, LNMCS5, LNMCS10 and LNMCS20 samples are provided in the Supporting Information.

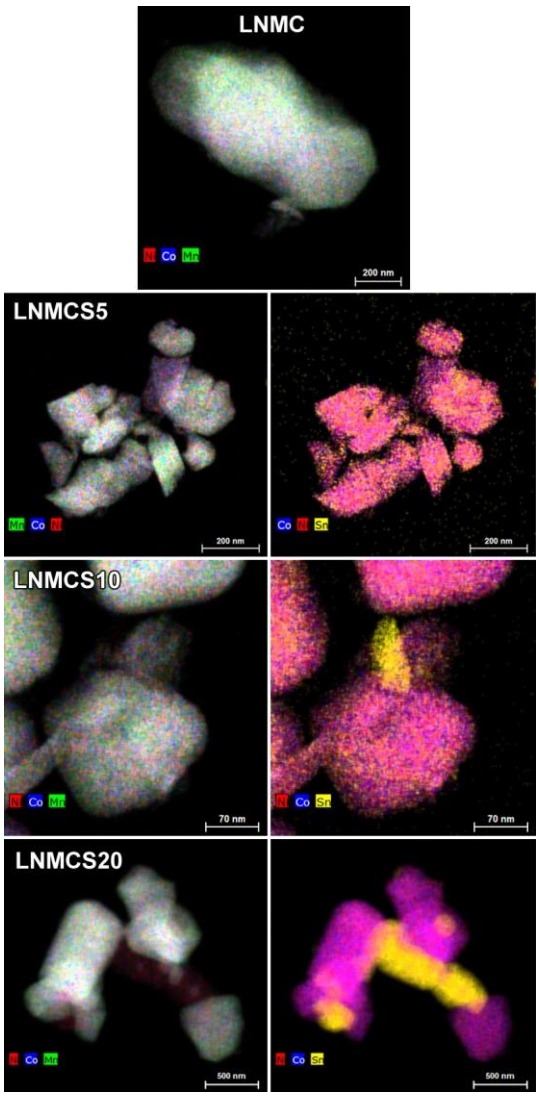

Fig. 2. Top: The mixed (Ni, Mn, Co) elemental maps of a representative LNMC (x=0) particle. Bottom: The mixed (Ni, Mn, Co) and (Ni, Co, Sn) elemental maps of respective particles of LNMCS5 (x=0.027), LNMCS10 (x=0.054) and LNMCS20 (x=0.108). The elemental maps are given in counts.

As the main phases of LNMCS5, LNMCS10 and LNMCS20 are comparable based on the STEM-EDX and PXRD investigation and as LNMCS10 and LNMCS20 are not a single phase, the further structural study is exclusively presented for LNMCS5 and the unsubstituted LNMC reference material. Moreover, the additional Sn-rich phase of LNMCS10 and LNMCS20 immediately turns amorphous under the electron beam, preventing its structural analysis via HAADF-STEM. As this admixture phase is believed to have no significant electrochemical activity within the probed potential window, mainly due to the very low content of nickel and cobalt and the redox inactivity of Sn^{4+}, no further characterization has been performed.

The crystal structure of LNMC and LNMCS5 was investigated by means of SAED, HAADF-STEM and ABF-STEM in order to probe the cation ordering and oxygen stacking. The HAADF-STEM images and corresponding SAED patterns along the [010], [100] and [110] direction are shown in respectively **Fig. 3.** and **Fig. 4.** The [010] SAED patterns of both materials are consistent with the O3-type layered structure without noticeable stacking faults in the close-packed arrangement of the oxygen layers. The intensity of the atom columns in the HAADF-STEM images is proportional to the atomic number of the elements ($I \sim Z^2$). Therefore, the bright dots in the [010] HAADF-STEM images correspond to the transition metal atom columns, while the atom columns of lithium and oxygen are too weak to be observed. There is no periodic variation in the brightness of the pairs of projected TM columns themselves. Ordering between Sn and Mn, Ni and Co would result in periodic brighter columns due to the considerable higher Z of Sn relative to the other three TM cations. Therefore, the HAADF-STEM images indicate that the Sn atoms are randomly distributed over the TM positions. In order to directly visualize the O3 cubic close-packed sequence of the oxygen layers, ABF-STEM images along the [010] orientation were acquired (Supporting information, **Fig. S3.**), where the intensity is proportional to $Z^{1/3}$ and thus more sensitive to elements with low Z compared to HAADF-STEM. The ABF-STEM images confirm the O3-type stacking. The [010]/[110] SAED patterns of both materials are characterized by sharp strong reflections with k = 3n and diffuse weaker spots in the $k \neq$ 3n reciprocal lattice rows that originate from "honeycomb" ordering of the TM, Sn and Li cations. These diffraction patterns are very typical for the LMR-NMC materials containing abundant stacking faults due to lateral displacements or rotation of the "honeycomb" layers. In the [100]/[110] HAADF-STEM images, the "honeycomb" ordering manifests itself by a prominent pattern of pairs of bright dots (i.e. atom columns of transition metals) with the interdot distance of ~0.14 nm, and less bright dots (i.e. atom column containing both Li and transition metals) in between. Thus the SAED patterns and HAADF-STEM images clearly demonstrate that the Sn for Mn substitution preserves the layered O3 structure and "honeycomb" cation ordering.

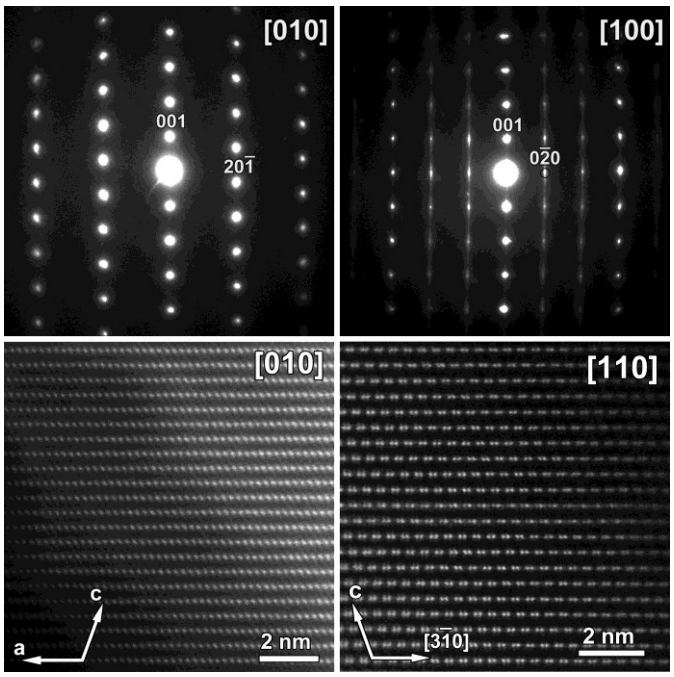

Fig. 3. Top: SAED patterns along the [010] and [100] orientation. Bottom: HAADF-STEM images along the [010] and [110] orientation. Both the SAED patterns and HAADF-STEM images are taken from LNMC.

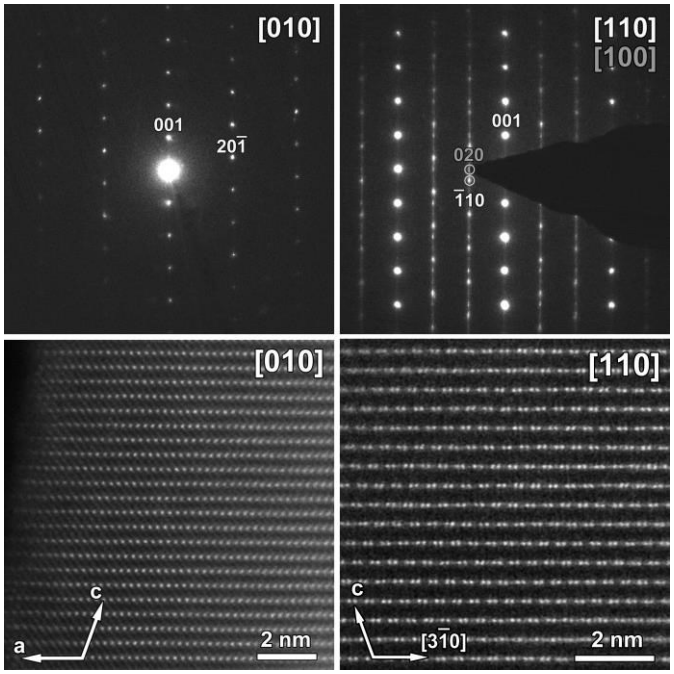

Fig. 4. Top: SAED patterns along the [010] and [110] orientation. Bottom: HAADF-STEM images along the [010] and [110] orientation. Both the SAED patterns and HAADF-STEM images are taken from LNMCS5.

In order to further investigate the Sn solubility in $Li_{1.2}Ni_{0.13}Co_{0.13}Mn_{0.54-x}Sn_xO_2$, the formation energies of Sn-substituted structures for a range of x-values have been calculated within the DFT framework. In an effort to reduce the computational complexity, the calculations were limited to $Li_{1.2}Mn_{0.80-x}Sn_xO_2$, which can be considered a reasonable strategy due to the similar ionic radii of Mn, Co and Ni, as well as the low concentration of Ni and Co. The solubility of Sn in this compound can be studied by considering the following decomposition reaction (Li_2SnO_3 corresponds to the admixture phase as detected by PXRD):

$$Li_{1.2}Mn_{0.8-x}Sn_xO_2 \rightarrow \left(1-\frac{x}{0.8}\right)\cdot Li_{1.2}Mn_{0.8}O_2 + \frac{x}{0.8}(0.6\cdot Li_2SnO_3 + 0.2\cdot SnO),$$

with formation energy:

$$E_f(x) = E(Li_{1.2}Mn_{0.8-x}Sn_xO_2) - \left(1-\frac{x}{0.8}\right)E(Li_{1.2}Mn_{0.8}O_2) - \frac{x}{0.8}[0.6\,E(Li_2SnO_3) + 0.2\,E(SnO)].$$

The limited solubility of Sn is confirmed by the DFT calculations. **Fig. 5.** shows the calculated formation energies for the Sn substituted structures compared to their decomposition in $Li_{1.2}Mn_{0.8}O_2$, Li_2SnO_3 and SnO. For the lowest Sn concentration, x = 0.042, the formation energy of the lowest energy configuration is only 6.5 meV/atom above the convex hull. This structure can reasonably be considered as metastable metastable(52) and as such the formation of a single phase is feasible at low Sn concentrations. However, as the Sn-concentration x is increased, the $Li_{1.2}Mn_{0.8-x}Sn_xO_2$ configurations become more unstable, increasing the likelihood of a decomposition in $Li_{1.2}Mn_{0.8}O_2$, Li_2SnO_3 and SnO phases, as observed in the PXRD results for the high Sn concentration samples. Note that if the Sn substituted orderings are generated randomly, i.e. without respecting the honeycomb pattern, the energies are significantly higher compared to the honeycomb structures at each Sn concentration. This matches the preservation of the honeycomb ordering for the Sn substituted structure found for the HAADF-STEM results.

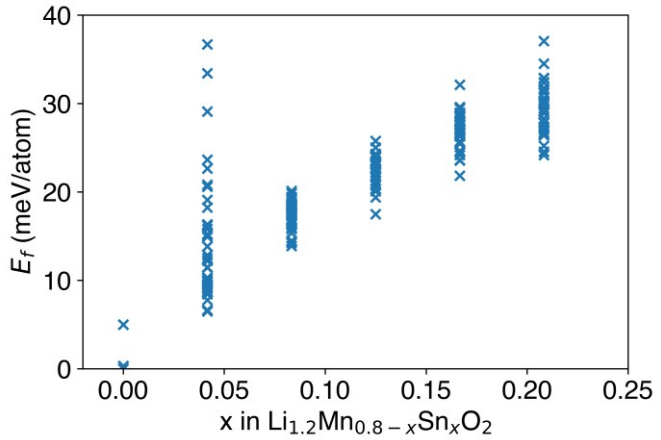

Fig. 5. Calculated formation energies of the Sn substituted structures for a range of Sn concentrations x. Within the 2x2x2 supercell, this corresponds to a set of 5 different values for x: {i/24 | i = 1, 2, 3, 4, 5}. Every mark corresponds to a symmetrically non-equivalent Li-Mn-Sn ordering at a specific Sn concentration.

Next to the metastability for low Sn dopant concentrations and instability for high Sn dopant concentrations as predicted by the DFT calculations as compared to decomposition in Li_2SnO_3, the synthesis process can also potentially influence the homogeneity and Sn substitution limit. A detailed investigation of the applied co-precipitation synthesis is reported in the next section in order to assess its consequence on the Sn substitution limit.

Synthesis

Hydroxide precipitation is a widespread method to prepare NMC precursors.(53)·(54)·(55)·(56)·(57) However, as nickel, manganese and cobalt are exclusively present in a 2+ oxidation state when precipitated as metal carbonates, carbonate precipitation synthesis is preferred over hydroxide precipitation methods for the synthesis of NMC with good control over metal oxidation states.(58)·(59)·(24)·(60) For example, Mn^{2+} is prone to oxidize to Mn^{3+}, forming MnO(OH), or even to oxidize to Mn^{4+}, precipitating as MnO_2.(59) The complexity of our system lies in the simultaneous addition of $SnSO_4$ whose precipitation conditions, especially in relationship with the Ni, Mn, Co sulfate precursors, is not well established yet. As a pH of 7.5 is known from literature to result in a homogeneous Ni, Co, Mn carbonate precipitate with metal stoichiometry equal to the elemental ratios between metal sulfate precursors(24), the pH value is adjusted to 7.5 by addition of diluted NH_3 or H_2SO_4. Besides, NH_3 acts as a complexing ligand, which could facilitate the formation of spherical particles(61)·(62)·(63)·(64)·(24).

The powder X-ray diffraction patterns of the intermediate samples NMC (x=0), NMCS5 (x=0.027), NMCS10 (x=0.054), NMCS20 (x=0.108) and NCS (x=0.54) recorded after co-precipitation, centrifugation and drying under vacuum at 75°C overnight are depicted in **Fig. 6.** Peak indexation is performed by aid of the PDF-2 2003 database. All peaks in the pattern of the NMC sample could be indexed using the targeted mixed Ni, Mn, Co carbonate phase. In the NMCS20 sample, additional peaks as marked by '+' are present, which are indexed as $Sn_6O_4(OH)_4$. For the NMCS10 and NMCS5 samples a single peak around 25° 2θ is observed, which, based on analogy with the observations made in NMCS20, is also attributed to the presence of $Sn_6O_4(OH)_4$. The absence of other peaks corresponding to the $Sn_6O_4(OH)_4$ phase is attributed to the low tin content. The NCS sample contains peaks assigned to $Sn_6O_4(OH)_4$, a mixed (Co, Ni) carbonate phase reflections and SnO. The latter marked by '*'.

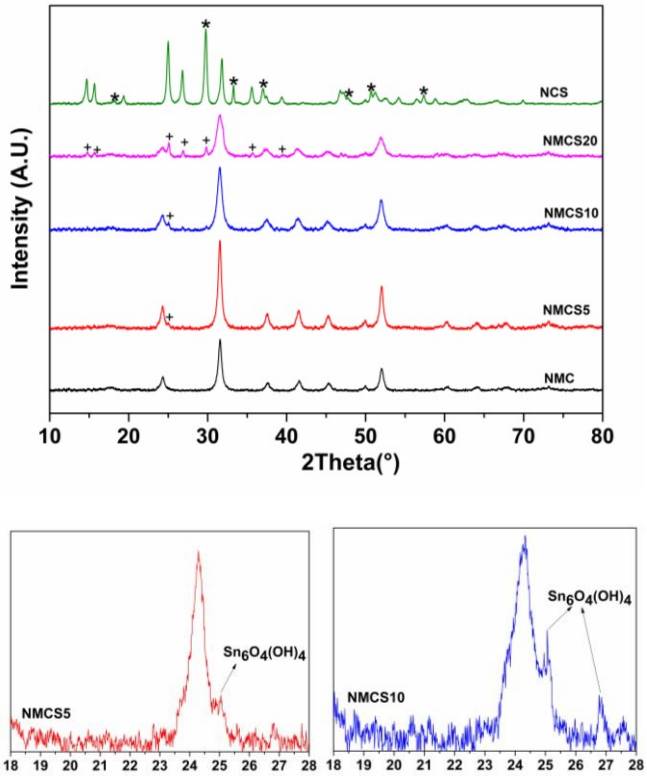

Fig. 6. Top: PXRD patterns of $Ni_{0.13}Co_{0.13}Mn_{0.54-x}(CO_3)_{0.8-x}$ – $(Sn_6O_4(OH)_4)_{x/6}$ (x=0, 0.027, 0.054, 0.108, 0.54). The main peaks of the $Sn_6O_4(OH)_4$ phase present for the NMCS5 (x=0.027), NMCS10 (x=0.054), NMCS20 (x=0.108) and NCS (x=0.54) samples are marked by '+'. Peaks indexed as SnO for the NCS sample are indicated with '*'. Bottom: Enlarged plots for NMCS10 and NMCS5 in the 18°-28° 2θ interval.

$Sn_6O_4(OH)_4$, consisting of $Sn_6O_4(OH)_4$ entities arranged in pseudo body-centred agglomerates interconnected by hydrogen bonds, is believed to be the only stable solid tin(II) hydroxide phase.(65) The addition of an excess of the precipitating agent Na_2CO_3 or adjusting the pH to a slightly acidic value of 6.8 for the x=0.108 composition still results in a predominant presence of the $Sn_6O_4(OH)_4$ phase based on PXRD measurements (Supporting Information, **Fig. S4.**). Also when using a different tin(II) salt, more specific $SnCl_2$, a $Sn_6O_4(OH)_4$ containing precipitate is formed after the addition of Na_2CO_3 as a precipitating agent in a basic (pH 8-10) aqueous medium(66). A possible explanation for the formation of SnO in the NCS sample can be found in the dehydration of $Sn_6O_4(OH)_4$ through ageing at room temperature(67).

In order to determine to which extent the transition metals and Sn are homogeneously distributed within the sample and to probe the metal composition, STEM-EDX has been performed on the NMC, NMCS5 and NMCS20 samples. The corresponding mixed elemental EDX maps are shown in **Fig. 7.** For the NMC sample the average transition metal composition is in agreement with the nominal stoichiometry $Ni_{0.13}Co_{0.13}Mn_{0.54}$. Next to the particles with a composition that is in agreement with the expected stoichiometry, also Ni-rich particles are detected for the NMC sample. The transition metals are moderately homogeneously distributed for most of the main phase particles. For both the NMCS5 and NMCS20 samples an inhomogeneous elemental distribution is obtained. Three different phases are observed: a main phase corresponding to the expected stoichiometry, a Sn-rich phase and a Ni-rich/Mn-poor phase. All three phases contain Ni, Mn, Co and Sn. Due to overlap of different phases, it turned out to be impossible to calculate the average composition for those three phases. The formation of a Sn-rich phase can be rationalized by the precipitation of Sn^{2+} as $Sn_6O_4(OH)_4$ and not as a mixed metal carbonate phase together with Ni^{2+}, Mn^{2+} and Co^{2+}.

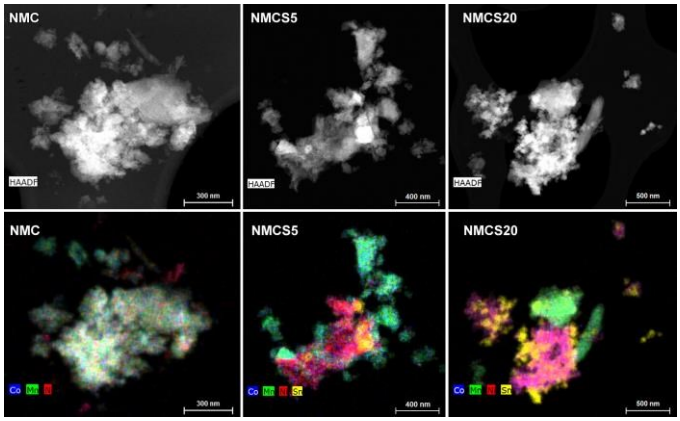

Fig. 7. HAADF-STEM of different particles together with left the mixed (Ni, Co, Mn) elemental map of NMC (x=0), in the middle the mixed (Co, Mn, Ni, Sn) elemental map of NMCS5 (x=0.027) and right the mixed (Co, Mn, Ni, Sn) elemental maps of NMCS20 (x=0.108). The element maps are given in counts.

In an attempt to probe the influence of the applied synthesis method on the formation of a Sn-rich phase, a sample named LNMCS20_b, consisting of $Li_{1.2}Ni_{0.13}Co_{0.13}Mn_{0.432}Sn_{0.108}O_2$, has been prepared via an aqueous citrato-based solution-gel method. The synthesis procedure is described in the Experimental section. A pre-calcined Li, TM, Sn (peroxo) citrato solution-gel precursor (hereafter named as LNMCS20_a) is heat-treated following the same procedure as for the Li-rich/Mn-rich intermediates obtained from the co-precipitation synthesis.

The mixed elemental maps of a representative particle of LNMCS20_a are depicted in **Fig. 8**. Ni and Co are homogeneously distributed. A variation of Mn and Sn within a range of 15 at.% is detected for the analyzed regions and particles. The TM and Sn are more homogeneously distributed for the solution-gel precursor as compared to the co-precipitation intermediate precursor NMCS20. The additional peaks related to a Sn-rich phase (most prominent peak at 18° 2θ) present in the PXRD pattern of LNMCS20_b presented in **Fig. 9.** further indicate that the formation of a Sn-rich phase is intrinsically related to the poor mixing of Sn with the TM in Li-rich/Mn-rich NMC.

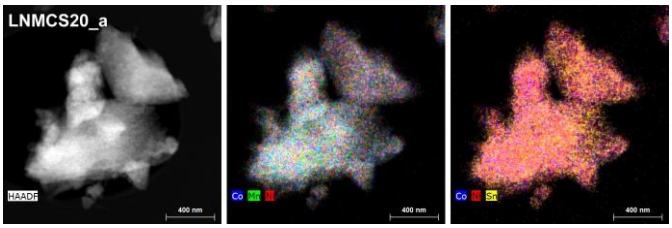

Fig. 8. HAADF-STEM of the representative LNMCS20_a particle together with in the middle the mixed (Co, Mn, Ni) elemental map and right the mixed (Co, Ni, Sn) elemental map. The element maps are given in counts.

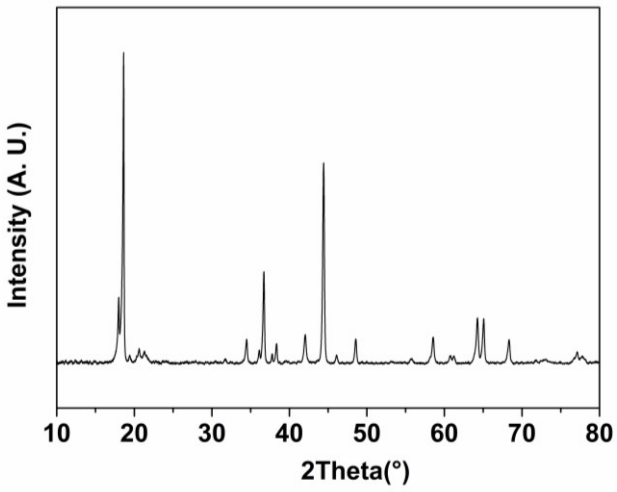

Fig. 9. PXRD pattern of the LNMCS20_b sample.

Electrochemical characterization

In order to comparatively assess voltage fade, galvanostatic cycling has been performed within the 3.00 V - 4.55 V vs. Li/Li^+ potential window on the LNMC and LNMCS5 samples. The lower potential limit has been set at 3.00 V, as voltage fade dominates in the ~3.1 - 3.3 V voltage interval for LMR-NMC(68). Selected charge/discharge curves are shown in **Fig. 10.** The slope region observed for both samples up to ~4.4 V is related to the oxidation of Ni^{2+} to Ni^{3+} and Ni^{4+} and Co^{3+} to Co^{4+}.(8) Evidence for anionic redox chemistry of the oxygen sublattice can be found for both samples in the potential plateau, observed at around 4.5 V vs. Li/Li^+ during the first charging step (Supporting Information, **Fig. S5.**).(69)·(70)·(71)·(25) By differential electrochemical mass spectrometry (DEMS) on ^{18}O-labelled $Li_{1.2}Ni_{0.13}Co_{0.13}Mn_{0.54}O_2$ it is shown by Luo et al.(15) that the 4.5 V plateau predominantly originates from hole formation on oxygen sites from the oxygen sublattice. Only a minor amount of released oxygen has been detected. Currently it is still under debate in

literature whether the released oxygen during the first charging step originates from the bulk lattice or from the near-surface region of the Li/Mn-rich NMC particles.(3),(70),(71),(25),(72) It was also shown by Luo et al. that holes formed at ~4.5 V are localized, no real O_2^{2-} species were detected.(15) The absence of O_2^{2-} species can also be rationalized by the finding that the required rotation of oxygen bonds to form peroxo-like species is inhibited by the directional bonds with oxygen of transition metals possessing partially occupied d orbitals.(73) Amongst the transition metal cations, localized hole formation on oxygen is most facilitated by Mn^{4+} as the Mn^{4+}-O bond is less covalent than Ni^{4+}-O or Co^{4+}-O. The Li^{+}-O bond is characterized by an even lower covalency than Mn^{4+}-O and by consequence contributes more to the localized hole formation on oxygen.(15) As Sn^{4+} has completely filled d orbitals, resulting in less directional bonds with oxygen, formation of peroxo-like species is more facilitated at ~4.5 V.(73) The voltage plateau depicted in **Fig. S5.** at around ~4.5 V is comparable for both unsubstituted LNMC and Sn substituted LNMCS5, both reaching capacities of ~250 mAh/g. Plausible explanations can be found in the low Sn^{4+} dopant concentration and/or in a potential formation of O-O bonds for oxygen in the direct vicinity of Sn^{4+}. For the subsequent 99 charge/discharge cycles, comparable voltage fade for both samples is observed, as presented in **Fig. 10.** A transition from layered to spinel-type structure upon extended cycling with upper cut-off potential of 4.55 V vs. Li/Li^{+} is expected to be hardly mitigated by replacement of a few molar percent of Mn^{4+} by Sn^{4+} in LMR-NMC, despite the lower tendency of Sn^{4+} to undergo O_h-T_h-O_h migration during galvanostatic cycling. In literature(35), lower voltage fade upon Sn doping is observed for fully charged LMR-NMC up to ~4.8 V vs. Li/Li^{+}. This can be potentially partly ascribed to a difference in tendency to fully oxidize oxygen (resulting in oxygen release from the oxygen sublattice) between oxygen possessing localized holes and O-O dimers.

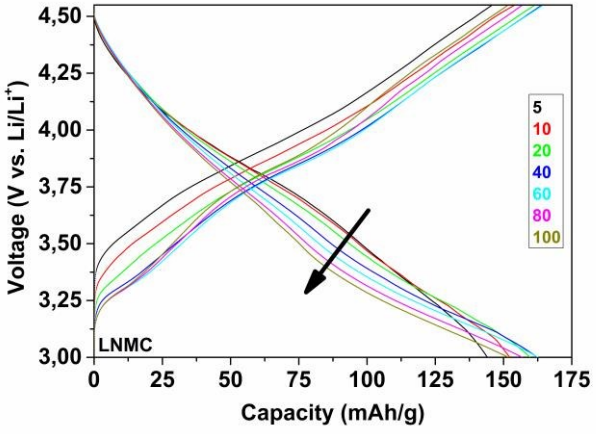

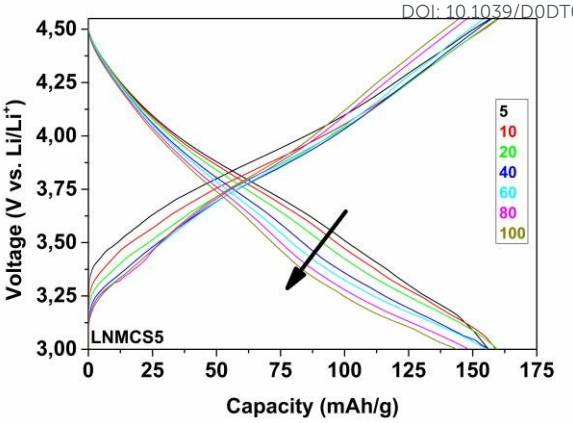

Fig. 10. Selected charge/discharge curves (cycle number is given in the legend) in the 3.00V-4.55V vs. Li/Li^{+} voltage window for LNMC and LNMCS5. Voltage fade is indicated by the arrow.

Conclusions

We have described the synthesis of $Li_{1.2}Ni_{0.13}Co_{0.13}Mn_{0.54-x}Sn_xO_2$ (x=0-0.54) via a facile aqueous co-precipitation method using sodium carbonate as a precipitating agent, followed by a thermal treatment. By PXRD and STEM-EDX it has been shown that the limited Sn^{4+} substitution degree not exceeding $x \approx 0.045$ in $Li_{1.2}Ni_{0.13}Co_{0.13}Mn_{0.54-x}Sn_xO_2$ is most probably intrinsically related to the structure of Li-rich/Mn-rich NMC and not to the intermediate $Sn_6O_4(OH)_4$ phase formed after co-precipitation. For x=0.054 and x=0.108 an additional Sn-rich phase is formed next to a Sn-doped Li-rich/Mn-rich main phase. The composition of the Sn-doped main phase is comparable for all the Sn substituted samples. The transition metals and Sn are homogeneously distributed in the Li-rich/Mn-rich phase, validating the quality of our applied synthesis method. Up to x=0.108, a highly crystalline, layered structure is formed, as confirmed by PXRD. A slight increase of the lattice parameters and volume is observed upon replacing 5% of Mn^{4+} by Sn^{4+}, in agreement with the larger ionic radius of Sn^{4+} as compared to Mn^{4+}. It is shown that honeycomb ordering is maintained upon replacing 5% of Mn^{4+} by Sn^{4+}.

For the first time to our knowledge, voltage fade has been assessed within a potential window with upper potential limited to only 4.55 V vs. Li/Li^{+}. Galvanostatic cycling have been performed on the x=0 and x=0.027 compositions. Both materials are characterized by discharge capacities around 140 mAh/g at C/10 for 100 cycles. Those results are in agreement with the similar structural properties of the x=0 and x=0.027 compositions based on our TEM and qualitative PXRD study. To conclude, we observed that, under our synthesis conditions, replacing a few molar percent of Mn^{4+} by Sn^{4+} in Li-rich/Mn-rich NMC is not considered a valuable strategy to significantly inhibit voltage fade upon extended galvanostatic cycling below the fully charged state. This is most probably related to the low substitution degree of Sn^{4+} in the LMR-NMC crystal structure and the inability of Sn^{4+} to inhibit the structural transition from a layered

structure to a spinel-type structure upon extended galvanostatic cycling.

Conflicts of interest

There are no conflicts to declare.

Acknowledgements

The authors acknowledge Research Foundation Flanders (FWO) project number G040116N for funding. The authors are grateful to Dr. Ken Elen and Greet Cuyvers (imo-imomec, UHasselt and imec) for respectively preliminary PXRD measurements and performing ICP-AES on the monometal precursors. Dr. Dmitry Rupasov (Skolkovo Institute of Science and Technology) is acknowledged for performing TGA measurements on the metal sulfate precursors. The computational resources and services used in this work were provided by the VSC (Flemish Supercomputer Center) and the HPC infrastructure of the University of Antwerp (CalcUA), both funded by the FWO-Vlaanderen and the Flemish Government-department EWI.

Notes and references

‡ Footnotes relating to the main text should appear here. These might include comments relevant to but not central to the matter under discussion, limited experimental and spectral data, and crystallographic data.

1. Deng ZQ, Manthiram A. Influence of Cationic Substitutions on the Oxygen Loss and Reversible Capacity of Lithium-Rich Layered Oxide Cathodes. Phys Chem C. 2011;115:7097–103.
2. Ates MN, Mukerjee S, Abraham KM. A high rate Li-rich layered MNC cathode material for lithium-ion batteries. RSC Adv [Internet]. 2015;5:27375–86. Available from: http://dx.doi.org/10.1039/C4RA17235C
3. Teufl T, Strehle B, Philipp M, Gasteiger HA, Mendez MA. Oxygen Release and Surface Degradation of Li- and Mn-Rich Layered Oxides in Variation of the Li2MnO3 Content. J Electrochem Soc. 2018;165(11):A2718–31.
4. Wang G, Meilin L. Li1.2Ni0.13Co0.13Mn0.54O2 with controllable morphology and size for high performance lithium-ion batteries. ACS Appl Mater Interfaces. 2017;9:24358–5368.
5. He Z, Wang Z, Che H, Huang Z, Li X, Guo H. Electrochemical performance of zirconium doped lithium rich layered Li1.2Mn0.54Ni0.13Co0.13O2 oxide with porous hollow structure. J Power Sources. 2015;299:334–41.
6. Zeng J, Cui Y, Qu D, Zhang Q, Wu J, Zhu X, et al. Facile Synthesis of Platelike Hierarchical Li1.2Mn0.54Ni0.13Co0.13O2 with Exposed {010} Planes for High-Rate and Long Cycling-Stable Lithium Ion Batteries. ACS Appl Mater Interfaces. 2016;8:26082–90.
7. Wei Z, Xia Y, Qiu B, Zhang Q, Han S, Liu Z. Correlation between transition metal ion migration and the voltage ranges of electrochemical process for lithium-rich manganese-based material. J Power Sources [Internet]. 2015;281:7–10. Available from: http://dx.doi.org/10.1016/j.jpowsour.2015.01.149
8. Koga H, Croguennec L, Mannessiez P, Bourgeois L, Duttine M, Suard E, et al. Li1.20Mn0.54Co0.13Ni0.13O2 with Different Particle Sizes as Attractive Positive Electrode Materials for Lithium‐Ion Batteries: Insights into Their Structure. J Phys Chem C. 2012;116:13497–506.
9. Assat G, Tarascon J. Fundamental understanding and practical challenges of anionic redox activity in Li-ion batteries. Nat Energy [Internet]. 2018;3:373–86. Available from: http://dx.doi.org/10.1038/s41560-018-0097-0
10. Koga H, Croguennec L, Me M. Operando X‐ray Absorption Study of the Redox Processes Involved upon Cycling of the Li-Rich Layered Oxide Li1.20Mn0.54Co0.13Ni0.13O2 in Li Ion Batteries. J Phys Chem C. 2014;118:5700–9.
11. Koga H, Croguennec L, Michel M, Bourgeois L, Suard E. Reversible Oxygen Participation to the Redox Processes Revealed for Li1.20Mn0.54Co0.13Ni0.13O2. J Electrochem Soc. 2013;160:A786–92.
12. Oishi M, Yogi C, Watanabe I, Ohta T, Orikasa Y, Uchimoto Y, et al. Direct observation of reversible charge compensation by oxygen ion in Li-rich manganese layered oxide positive electrode material, Li1.16Ni0.15Co0.19Mn0.50O2. J Power Sources [Internet]. 2015;276:89–94. Available from: http://dx.doi.org/10.1016/j.jpowsour.2014.11.104
13. Assat G, Iadecola A, Delacourt C. Decoupling Cationic – Anionic Redox Processes in a Model Li-Rich Cathode via Operando X ‐ ray Absorption Spectroscopy. Chem Mater. 2017;29:9714–24.
14. Shimoda K, Minato T, Nakanishi K, Komatsu H, Matsunaga T, Tanida H, et al. Oxidation behaviour of lattice oxygen in Li-rich manganese-based layered oxide studied by hard X-ray photoelectron spectroscopy. J Mater Chem A. 2016;4:5909–16.
15. Luo K, Roberts MR, Hao R, Guerrini N, Pickup DM, Liu Y, et al. Charge-compensation in 3d-transition-metal- oxide intercalation cathodes through the generation of localized electron holes on oxygen. Nat Chem [Internet]. 2016;8:684–91. Available from: http://dx.doi.org/10.1038/nchem.2471
16. Foix D, Sathiya M, Mccalla E, Tarascon J, Gonbeau D. X - ray Photoemission Spectroscopy Study of Cationic and Anionic Redox Processes in High-Capacity Li-Ion Battery Layered-Oxide Electrodes. J Phys Chem C. 2016;120:862–74.
17. Assat G, Foix D, Delacourt C, Iadecola A, Dedryvère R, Tarascon J. Fundamental interplay between anionic/cationic redox governing the kinetics and thermodynamics of lithium-rich cathodes. Nat Commun [Internet]. 2017;8:1–12. Available from: http://dx.doi.org/10.1038/s41467-017-02291-9
18. Yahia M Ben, Vergent J, Saubanère M, Doublet M-L. Unified picture of anionic redox in Li/Na-ion batteries. Nat Mater. 2019;18:496–502.
19. Saubanère M, McCalla E, Tarascon J-M, Doublet M-L. The

intriguing question of anionic redox in high-energy density cathodes for Li-ion batteries. Energy Environ Sci. 2016;9:984–91.

20. McCalla E, Abakumov A. M, Saubanère M, Foix D, Berg EJ, Rousse G, et al. Visualization of O-O peroxo-like dimers in high-capacity layered oxides for Li-ion batteries. Science (80-). 2015;350(6267):1516–21.
21. Hong J, Gent WE, Xiao P, Lim K, Seo D, Wu J, et al. Metal–oxygen decoordination stabilizes anion redox in Li-rich oxides. Nat Mater [Internet]. 2019;18:256–265. Available from: http://dx.doi.org/10.1038/s41563-018-0276-1
22. Li L, Castro FC, Park JS, Li H, Lee E, Boyko TD, et al. Probing Electrochemically Induced Structural Evolution and Oxygen Redox Reactions in Layered Lithium Iridate. Chem Mater. 2019;31:4341–52.
23. Sathiya M, Abakumov AM, Foix D, Rousse G, Ramesha K, Saubanère M, et al. Origin of voltage decay in high-capacity layered oxide electrodes. Nat Mater. 2015;14:230–8.
24. Pimenta V, Sathiya M, Batuk D, Abakumov AM, Giaume D, Cassaignon S, et al. Synthesis of Li-Rich NMC : A Comprehensive Study. Chem Mater. 2017;29:9923–36.
25. Yabuuchi N, Yoshii K, Myung S, Nakai I, Komaba S. Detailed Studies of a High-Capacity Electrode Material for Rechargeable Batteries, Li2MnO3-LiCo1/3Ni1/3Mn1/3O2. J Am Chem Soc. 2011;133:4404–19.
26. Mohanty D, Li J, Abraham DP, Payzant EA, Wood DL, Daniel C. Unraveling the Voltage-Fade Mechanism in High-Energy-Density Lithium-Ion Batteries: Origin of the Tetrahedral Cations for Spinel Conversion. Chem Mater. 2014;26:6272–80.
27. Zheng J, Pinghong X, Meng G, Xiao J, Browing ND, Yan P, et al. Structural and Chemical Evolution of Li- and Mn-Rich Layered Cathode Material. Chem Mater. 2015;27:1381–90.
28. Ito A, Shoda K, Sato Y, Hatano M, Horie H, Ohsawa Y. Direct observation of the partial formation of a framework structure for Li-rich layered cathode material Li[Ni0.17Li0.2Co0.07Mn0.56]O2 upon the first charge and discharge. J Power Sources [Internet]. 2011;196:4785–90. Available from: http://dx.doi.org/10.1016/j.jpowsour.2010.12.079
29. Croy JR, Balasubramanian M, Gallagher KG, Burrell AK. Review of the U.S. Department of Energy ' s " Deep Dive " E ff ort to Understand Voltage Fade in Li- and Mn-Rich Cathodes. Acc Chem Res. 2015;48:2813–21.
30. Benedek R, Iddir H. Simulation of First-Charge Oxygen-Dimerization and Mn-Migration in Li-Rich Layered Oxides xLi2MnO3·(1 − x)LiMO2 and Implications for Voltage Fade. J Phys Chem C. 2017;121:6492–9.
31. Kang G. The Effects of Incorporated Sn in Resynthesized Ni-Rich Cathode Materials on Their Lithium-Ion Battery Performance. Metals (Basel). 2017;7.
32. Lu Y, Pang M, Shi S, Ye Q, Tian Z, Wang T. Enhanced Electrochemical Properties of Zr4+-doped Material for Lithium-ion Battery at Elevated Temperature. Sci Rep. 2018;8(2981):1–14.
33. Sathiya M, Rousse G, Ramesha K, Laisa CP, Vezin H, Sougrati MT, et al. Reversible anionic redox chemistry in high-capacity layered-oxide electrodes. Nat Mater [Internet]. 2013;12(7):1–9. Available from: http://dx.doi.org/10.1038/nmat3699
34. Qiao Q, Qin L, Li G, Wang Y, Gao X. Sn-stabilized Li-rich layered Li(Li0.17Ni0.25Mn0.58)O2 oxide as a cathode for advanced lithium-ion batteries. J Mater Chem A Mater energy Sustain [Internet]. 2015;3:17627–34. Available from: http://dx.doi.org/10.1039/C5TA03415A
35. Zhou L, Liu J, Huang L, Jiang N, Zheng Q, Lin D. Sn-doped Li1.2Mn0.54Ni0.13Co0.13O2 cathode materials for lithium-ion batteries with enhanced electrochemical performance. J Solid State Electrochem. 2017;21(12):3467–77.
36. Stanulis A, Hardy A, De Dobbelaere C, D'Haen J, Van Bael M, Kareiva A. SnO2 thin films from an aqueous citrato peroxo Sn (IV) precursor. J Sol-Gel Sci Technol. 2012;(62):57–64.
37. Petříček V, Dušek M, Palatinus L. Crystallographic Computing System JANA2006 : General features. Z Krist 2014. 2014;229(5):345–52.
38. Hart GLW, Graf PA, Kim K, Jones WB. Direct enumeration of alloy configurations for electronic structural properties. Appl Phys Lett. 2005;87(24):1–3.
39. Hart GLW, Forcade RW. Generating derivative structures from multilattices: Algorithm and application to hcp alloys. Phys Rev B. 2009 Jul;80(1).
40. Morgan WS, Hart GLW, Forcade RW. Generating derivative superstructures for systems with high configurational freedom. Comput Mater Sci. 2017 Aug;136:144–9.
41. Jain A, Ong SP, Chen W, Medasani B, Qu X, Kocher M, et al. Fireworks: A dynamic workflow system designed for highthroughput applications. Concurr Comput. 2015 Dec;27(17):5037–59.
42. Kresse G, Hafner J. Ab initio molecular dynamics for liquid metals. Phys Rev B. 1992 Jan;47(1):558–61.
43. Joubert D. From ultrasoft pseudopotentials to the projector augmented-wave method. Phys Rev B - Condens Matter Mater Phys. 1999 Jan;59(3):1758–75.
44. Kresse G, Furthmüller J. Efficiency of ab-initio total energy calculations for metals and semiconductors using a plane-wave basis set. Comput Mater Sci. 1996 Jul;6(1):15–50.
45. Blöchl PE. Projector augmented-wave method. Phys Rev B. 1994 Dec;50(24):17953–79.
46. Sun J, Ruzsinszky A, Perdew J. Strongly Constrained and Appropriately Normed Semilocal Density Functional. Phys Rev Lett. 2015 Jul;115(3):36402.
47. Peng H, Yang Z-H, Perdew JP, Sun J. Versatile van der Waals Density Functional Based on a Meta-Generalized Gradient Approximation. Phys Rev X. 2016 Oct;6(4).
48. Govaerts K, Saniz R, Partoens B, Lamoen D. van der Waals bonding and the quasiparticle band structure of {SnO} from first principles. Phys Rev B. 2013 Jun;87(23).
49. Monkhorst HJ, Pack JD. Special points for Brillouin-zone integrations. Phys Rev B. 1976 Jun;13(12):5188–92.
50. Blöchl PE, Jepsen O, Andersen OK. Improved tetrahedron method for Brillouin-zone integrations. Phys Rev B. 1994 Jun;49(23):16223–33.
51. Mou J, Deng Y, Song Z, Zheng Q, Lam KH, Lin D. Excellent

rate capability and cycling stability in Li+- conductive Li2SnO3-coated LiNi0.5Mn1.5O4 cathode materials for lithium-ion batteries. Dalt Trans. 2018;47:7020–8.

52. Sun W, Dacek ST, Ong SP, Hautier G, Jain A, Richards WD, et al. The thermodynamic scale of inorganic crystalline metastability. Sci Adv. 2016 Nov;2(11):e1600225.
53. Bommel A Van, Dahn JR. Analysis of the Growth Mechanism of Coprecipitated Spherical and Dense Nickel , Manganese , and Cobalt-Containing Hydroxides in the Presence of Aqueous Ammonia. Chem Mater. 2009;21:1500–3.
54. Luo X, Wang X, Liao L, Gamboa S, Sebastian PJ. Synthesis and characterization of high tap-density layered Li[Ni1/3Co1/3Mn1/3]O2 cathode material via hydroxide co-precipitation. J Power Sources. 2006;158:654–8.
55. Lee M, Kang Y, Myung S, Sun Y. Synthetic optimization of Li [Ni1/3Co1/3 Mn1/3]O2 via co-precipitation. Electrochim Acta. 2004;50:939–48.
56. Chen Y, Xu G, Li J, Zhang Y, Chen Z, Kang F. High capacity 0.5Li2MnO3·0.5LiNi0.33Co0.33Mn0.33O2 cathode material via a fast co-precipitation method. Electrochim Acta [Internet]. 2013;87:686–92. Available from: http://dx.doi.org/10.1016/j.electacta.2012.09.024
57. Zhou Y, Wang Y, Li S, Mei J, Liu H, Liu H, et al. Irregular micro-sized Li1.2Mn0.54Ni0.13Co0.13O2 particles as cathode material with a high volumetric capacity for Li-ion batteries. J Alloys Compd [Internet]. 2017;695:2951–8. Available from: http://dx.doi.org/10.1016/j.jallcom.2016.11.375
58. Xiang Y, Yin Z, Li X. Synthesis and characterization of manganese- , nickel- , and cobalt-containing carbonate precursors for high capacity Li-ion battery cathodes. J Solid State Electrochem. 2014;18:2123.
59. Wang D, Belharouak I, Koenig GM, Amine K. Growth mechanism of Ni0.3Mn0.7CO3 precursor for high capacity Li-ion battery cathodes. J Mater Chem. 2011;21:9290–5.
60. Li Y, Mei J, Guo X, Zhong B, Liu H, Liu G, et al. Hollow Li1.2Mn0.54Ni0.13Co0.13O2 micro-spheres synthesized by a co-precipitation method as a high-performance cathode material for Li-ion batteries. RSC Adv [Internet]. 2016;6:70091–8. Available from: http://dx.doi.org/10.1039/C6RA13265K
61. Belharouak I, Sun YK, Amine K. Physical and electrochemical properties of spherical Li1+x(Ni1/3Co1/3Mn1/3)1−xO2 cathode materials. J Power Sources. 2008;177:177–83.
62. Zhang S, Deng C, Fu BL, Yang SY, Ma L. Synthetic optimization of spherical Li[Ni1/3Mn1/3Co1/3]O2 prepared by a carbonate co-precipitation method. Powder Technol [Internet]. 2010;198(3):373–80. Available from: http://dx.doi.org/10.1016/j.powtec.2009.12.002
63. Deng C, Zhang S, Ma L, Sun YH, Yang SY, Fu BL, et al. Effects of precipitator on the morphological, structural and electrochemical characteristics of Li[Ni1/3Co1/3Mn1/3]O2 prepared via carbonate coprecipitation. J Alloy Compd. 2011;509:1322–7.
64. Myung S, Lee M, Komaba S, Kumagai N, Sun Y. Hydrothermal synthesis of layered Li[Ni1/3Co1/3Mn1/3]O2 as positive electrode material for lithium secondary battery. Electrochim Acta. 2005;50:4800–6.
65. Khanderi J, Shi L, Rothenberger A. Hydrolysis of bis(dimethylamido)tin to tin (II) oxyhydroxide and its selective transformation into tin (II) or tin (IV) oxide. Inorg Chim Acta. 2014;427:27–32.
66. Kuznetsova SA, Pichugina AA. Synthesis and Properties of SnO Prepared from Ammoniacal and Carbonate Suspensions of Tin(II) Hydroxy Compound under Microwave Radiation. Russ J Appl Chem. 2015;88(6):1082–5.
67. Ghosh S, Roy S. Effect of ageing on Sn6O4(OH)4 in aqueous medium—simultaneous production of SnO and SnO2 nanoparticles at room temperature. J Sol-Gel Sci Technol. 2017;81:769–73.
68. Gallagher KG, Croy JR, Balasubramanian M, Bettge M, Abraham DP, Burrell AK, et al. Correlating hysteresis and voltage fade in lithium- and manganese-rich layered transition-metal oxide electrodes. Electrochem commun [Internet]. 2013;33:96–8. Available from: http://dx.doi.org/10.1016/j.elecom.2013.04.022
69. Hou X, Huang Y, Ma S, Zou X, Hu S. Facile hydrothermal method synthesis of coralline-like materials for lithium-ion batteries. Mater Res Bull [Internet]. 2015;63:256–64. Available from: http://dx.doi.org/10.1016/j.materresbull.2014.12.011
70. Lanz P, Sommer H, Schulz-dobrick M, Novák P. Oxygen release from high-energy xLi2MnO3·(1 − x)LiMO2 (M = Mn, Ni, Co): Electrochemical, differential electrochemical mass spectrometric, in situ pressure, and in situ temperature characterization. Electrochim Acta [Internet]. 2013;93:114–9. Available from: http://dx.doi.org/10.1016/j.electacta.2013.01.105
71. Lu Z, Beaulieu LY, Donaberger RA, Thomas CL. Synthesis, Structure, and Electrochemical Behavior of Li[NixLi1/3-2x/3Mn2/3-x/3]O2. J Electrochem Soc. 2002;149(6):A778–91.
72. Strehle B, Kleiner K, Jung R, Chesneau F, Mendez M, Gasteiger HA, et al. The Role of Oxygen Release from Li- and Mn-Rich Layered Oxides during the First Cycles Investigated by On-Line Electrochemical Mass Spectrometry. J Electrochem Soc. 2017;164(2):A400–6.
73. Seo D-H, Lee J, Urban A, Malik R, Kang S, Ceder G. The structural and chemical origin of the oxygen redox activity in layered and cation-disordered Li-excess cathode materials. Nat Chem. 2016 Jul;8(7):692–7.